applied sciences

MDPI

Article

Efficient Implementation of Polymer Microwave Fiber Links Employing Non-Galvanic Coupling Mechanism

Vasileios Liakonis [1,*], Yannis Papananos [1], Franz Dielacher [2], Maciej Wojnowski [2] and Walter Hartner [2]

[1] School of Electrical and Computer Engineering, National Technical University of Athens, 157 72 Zografou, Greece; papan@elab.ntua.gr

[2] Infineon Technologies AG, 85579 Neubiberg, Germany; franz.dielacher@ieee.org (F.D.); maciej.wojnowski@infineon.com (M.W.); walter.hartner@infineon.com (W.H.)

* Correspondence: valiakonis@gmail.com

Abstract: In this paper, the performance, advantages and challenges of polymer microwave fibers (PMF) for sub-THz links are evaluated first. Then, a simple and elegant transceiver-integrated circuit (IC) and PMF wireless coupling scheme is presented. The proposed solution utilizes an advanced IC packaging technology to implement a Vivaldi antenna-in-package (AiP). The antenna is designed to provide lateral radiation and excellent directivity, so the proposed solution is very simple, compact, robust and cost-efficient: the IC readily connects to the PMF and the coupling is merely achieved by the packaged IC, without the need for any extra interface. The system operates at around 140 GHz, achieving a coupling loss of just 3.5 dB.

Keywords: advanced IC packaging; antenna-in-package (AiP); high data rate; polymer microwave fiber (PMF); Vivaldi antenna; embedded wafer level ball grid array (eWLB)

1. Introduction

Modern communication concepts such as those required for IoT and fully autonomous vehicles demand high volumes of data transmission. The ever-improving semiconductor technology offers the opportunity for high-data-rate wireless and non-wireless systems utilizing higher carrier frequencies in the sub-THz frequency domain [1–3]. For wireline communication links, two major solutions exist: copper and optical. For very long-distance and very high-speed links, expensive optical fiber solutions prevail. For medium–long-range links and low to medium speeds, copper is the most cost-efficient solution.

On the other hand, when it comes to low/medium distances and high data rates, the optical fiber becomes an expensive solution, whereas copper-based wired links are limited due to the increased impact of the skin effect at high frequencies [4]. Figure 1 clearly shows the limits of copper-based wired links, as a bit rate of 10 Gbps is impossible for a link longer than 5 m. Active copper cables can overcome the speed limitations [5]. However, they are hindered by energy efficiency limitations as the energy per bit rises over medium-distance links. The dielectric fiber waveguides proposed in recent years [6–22] provide an attractive and efficient solution, as shown in Figure 2.

Polymer fibers are very cheap and easy to produce, while they exhibit dielectric losses that are significantly smaller than those of their copper counterparts for short- and medium-range distances. Operation in the sub-THz frequency band (0.1–0.4 THz) is feasible and efficient through the polymer waveguide, while the attenuation is in the 1–5 dB/m range [6]. The extremely high carrier frequency guarantees very broadband communication channels, and this, in combination with the low attenuation and dispersion properties of the polymer

Academic Editor: John Xiupu Zhang

Received: 22 December 2024
Revised: 30 January 2025
Accepted: 5 February 2025
Published: 11 February 2025

Citation: Liakonis, V.; Papananos, Y.; Dielacher, F.; Wojnowski, M.; Hartner, W. Efficient Implementation of Polymer Microwave Fiber Links Employing Non-Galvanic Coupling Mechanism. *Appl. Sci.* **2025**, *15*, 1824. https://doi.org/10.3390/app15041824

fibers, ensures high data rates (in the range of 10 Gbps and beyond). It is worth noting that PMF links are applicable not just in the field of telecommunications but also in remote sensing, as discussed in reference [20].

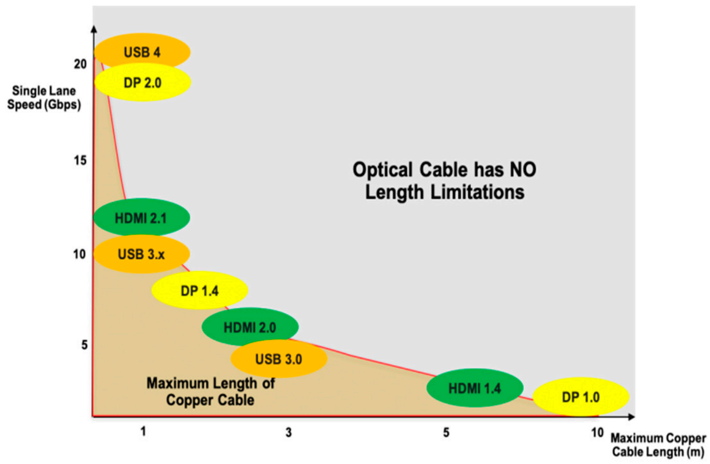

Figure 1. Bit rate vs. maximum cable length of a single copper wireline [5].

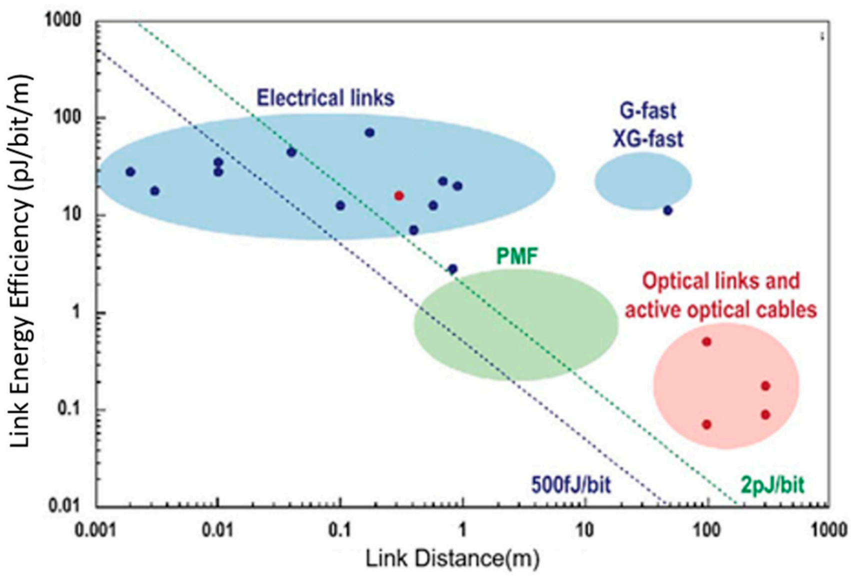

Figure 2. Bit energy per meter versus the maximum reach of commercial and research electrical links (blue diamonds) and commercial optical links (red circles) [23].

A key issue in the implementation of a polymer fiber waveguide solution is the way in which the fiber is coupled to the signal source/sink, i.e., the IC RF frontend. Various solutions have been proposed for this, including a micromachined interface and a wireless interface [8–11,18]. In all cases, the setup is either complex or suffers from mechanical stability issues and/or poor electrical performance.

In this paper, an overview of the performance of various polymer microwave fiber geometries is presented and evaluated first. Next, emphasis is placed on the wireless coupling solutions between the transceiver IC and the PMF. To this end, a compact, robust and very cost-efficient implementation is proposed, employing an antenna-in-package (AiP).

This paper is organized as follows. Section 1 presents a short introduction regarding the need for polymer microwave fiber (PMF) links, as well as our proposed implementation. In Section 2, an overview of polymer microwave fibers is presented, where we discuss how the design factors of the PMF affect its performance. In Section 3, the design process of the proposed coupling structure is shown, along with the results of EM simulations.

In Section 4, we demonstrate the measurements of the implemented coupling structure between the PMF and the IC. Lastly, Section 5 draws the conclusions.

2. PMF Overview

This section explores the materials and manufacturing processes used in PMFs, along with their propagation characteristics and electrical performance. Additionally, simulation results are presented to evaluate the PMF's effectiveness in various applications.

2.1. PMF Materials and Processes

The polymer microwave fiber or PMF can provide a directional transmission channel for mm-wave transmission and decrease the path loss significantly. It can be regarded as a unique type of dielectric waveguide that is flexible, cheap and usually produced from polymers such as polystyrene, polyethylene, polypropylene and Teflon (PTFE) [24]. These polymer materials have, as a common attribute, a low dielectric loss tangent in the order of 10^{-4} and a relatively low relative dielectric constant between 2 and 3, which makes them a perfect candidate for sub-mm-wave applications. Lower or higher relative dielectric constants lead to a larger or smaller PMF cross-section, respectively. Moreover, polymer materials exhibit very low material dispersion, which enables the use of PMFs for broadband links.

In conclusion, due to the aforementioned design process, the PMF allows a data link with more relaxed mechanical tolerances, leading to a more robust, lower-cost product.

2.2. PMF Propagation Characteristics

The key measures of a PMF's electrical performance are the attenuation and dispersion. The attenuation reflects the power losses inside the dielectric, while the dispersion reflects the phase distortion of the propagating modes.

2.2.1. Attenuation

The attenuation of a PMF is affected by multiple factors. For a given frequency band, the attenuation constant depends on the geometry and the material of the PMF. Consequently, a PMF is designed to operate in a specific frequency band. Moreover, for a given geometry, the attenuation of the PMF is frequency-dependent. As the frequency increases, the attenuation increases as well. Moreover, the attenuation is affected by the dielectric loss tangent of the core and cladding materials, although the core material has a higher impact on the attenuation, as most of the field is propagating inside the core.

To minimize the attenuation of the PMF, we must consider two key aspects of the waveguide's design. First, we must select a material with a low dielectric loss tangent. Second, we need to find the ideal conditions of operation, where the attenuation is at its lowest value, while, simultaneously, good field confinement is obtained. This can be achieved by carefully adjusting the cross-sectional area of the PMF. In Equation (1), the attenuation of a PMF is shown [25,26]:

$$a = \pi R \frac{f}{c} \tan\delta \left[\frac{\text{Nepper}}{\text{m}}\right] \quad (1)$$

where R is the geometric loss factor and shows how the field confinement affects the attenuation. As the field is concentrated inside the core (the geometric loss factor becomes higher), the attenuation increases. However, the waveguide is less prone to bending and other mechanical strains, which is very important for practical applications. An example with two rectangular PMFs of different cross-sectional areas at 140 GHz is shown in

Figure 3a,b, respectively. The PMF with the larger cross-sectional area (Figure 3a) exhibits stronger field confinement, as described earlier.

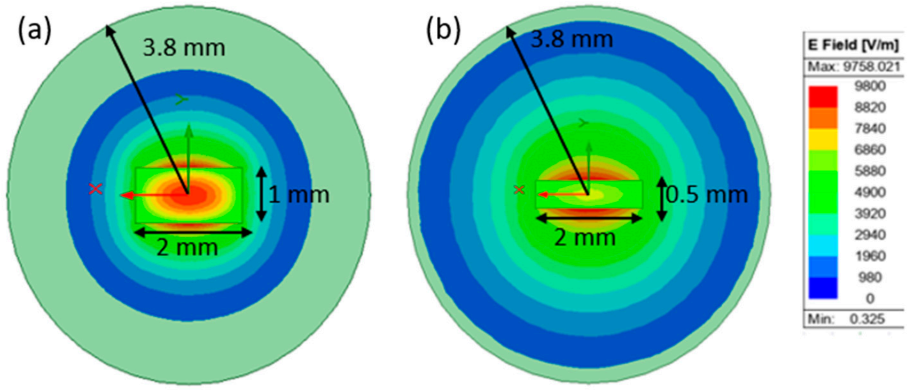

Figure 3. E-field distribution of a rectangular cross-section core PMF: (**a**) 2 mm × 1 mm and (**b**) 2 mm × 0.5 mm.

2.2.2. Dispersion

In PMFs, three types of dispersion are usually considered [13]: waveguide dispersion, material dispersion and modal dispersion. Waveguide dispersion occurs when a nonlinear change in the phase constant of the propagating wave is present. This is observed for every propagating mode of the PMF near its cutoff frequency. To avoid this nonlinearity in the dominant mode of propagation, the PMF must operate at a frequency band that is far from the cutoff frequency of the dominant mode. To further reduce waveguide dispersion, more complex methods can be implemented. Material dispersion is an intrinsic property of the dielectric, where the dielectric constant of the material varies over the frequency. For dielectric materials such as PTFE, polyethylene or ceramics, the dielectric characteristics—the permittivity and the dielectric loss tangent—are relatively constant over a large band of frequencies [25,26]. Finally, modal dispersion occurs when multiple modes exist in the waveguide. This kind of dispersion is very important as it introduces a tradeoff between multi-mode and single-mode operation. On one hand, by operating the PMF in a single mode, we limit the effective bandwidth of the structure, and the system is more prone to waveguide dispersion. On the other hand, by allowing multiple modes to propagate in the PMF, we achieve a higher bandwidth and lower waveguide dispersion for the dominant mode, but we introduce modal dispersion due to the different group delays of each mode.

2.3. PMF Electrical Performance Simulation Results

By utilizing one of the aforementioned polymer materials, the attenuation of an appropriately designed PMF is less dependent on its structure selection, as the inherently low dielectric tangent of such materials guarantees low-loss propagation. However, the dispersion and field confinement of the PMF are strongly influenced by the PMF's geometry. To demonstrate this, we present an investigation of the performance of various PMF structures.

The four examples that we choose to present are based on common dielectric waveguide geometries, such as the cylindrical dielectric rod [4] and the rectangular cross-section dielectric [27]. More specifically, the following geometries are considered: (1) a hollow-core cylindrical PMF; (2) a hollow-core rectangular PMF; (3) a solid-core rectangular PMF; and (4) a ribbon PMF. These four PMF geometries are depicted in Figure 4.

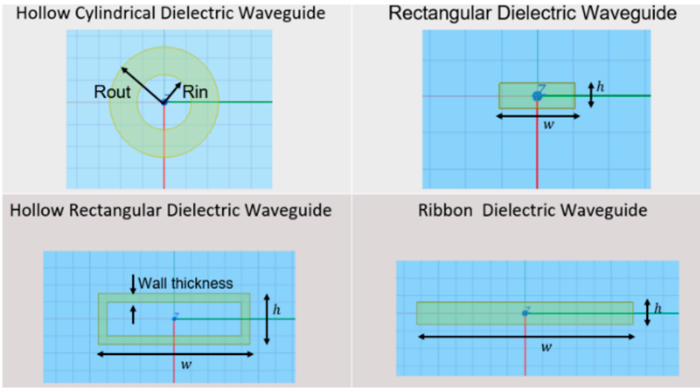

Figure 4. PMF cores evaluated.

All four PMF structures consist of a polyethylene core ($\varepsilon_r = 2.35$ and tan$\delta = 8 \times 10^{-5}$) and foam polyethylene cladding ($\varepsilon_r = 1.36$ and tan$\delta = 5 \times 10^{-5}$) and are designed for single-mode operation in the 110–170 GHz band. In Table 1, the PMFs' core dimensions are shown, while each PMF has cladding with a 6.8 mm diameter. All simulations were executed in the ANSYS HFSS 3D EM simulator.

Table 1. Dimensions of the PMF geometries.

PMF Structure	Dimensions
Hollow-core cylindrical PMF	*Rin* = 0.5 mm *Rout* = 1 mm
Hollow-core rectangular PMF	*h* = 0.6 mm *w* = 2.4 mm *wall thickness* = 150 µm
Solid-core rectangular PMF	*h* = 0.5 mm *w* = 2 mm
Ribbon PMF	*w* = 3.2 mm *h* = 0.32 mm

In Figure 5, the attenuation and the group delay of the four structures are shown, in TE11 mode for the three rectangular cross-sections and HE11 mode for the circular cross-section. In the single-mode region of operation, weaker field confinement, as shown for the hollow-core rectangular PMF, leads to lower attenuation and group velocity dispersion (GVD), as most of the guided wave's power is propagating in free space. However, a strongly confined field offers much better coupling in terms of insertion loss, which overpowers the small increase in attenuation and dispersion.

It is important to note that the rectangular cross-section PMF supports two families of modes. For this analysis, only the TE-like mode family was investigated, for two main reasons: (1) the TM-like modes are suppressed due to the coupling mechanism (as will be shown later in this paper) and (2) the two mode families are orthogonal to each other, meaning that the TM-like modes do not affect the performance of the TE-like modes, and vice versa, in terms of dispersion. This is based on Marcatili's assumption [27], which states that the Ex component of the TE-like modes is greater than the Ey component, which is approximately zero, and vice versa for the TM-like modes. This causes the orthogonality of the two mode families and, as a result, allows for full duplex links in rectangular PMFs [15].

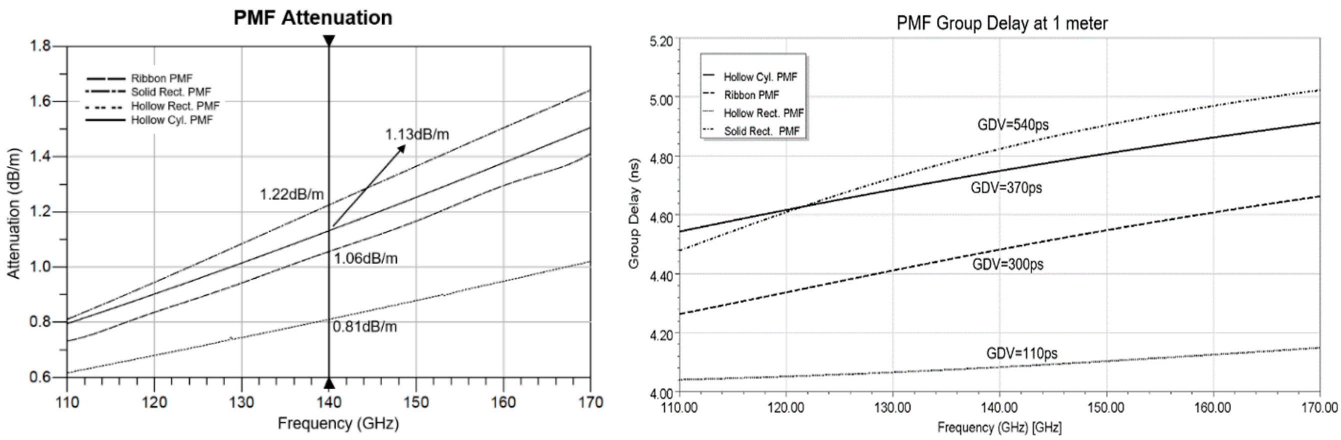

Figure 5. Simulation results in terms of the PMF attenuation and group delay, including the delta of the group delay (group delay variation or GDV).

All four PMF structures exhibit similar attenuation, but the field confinement of each structure introduces a tradeoff between the group delay variation and coupling robustness. As we will see later in this paper, the solid-core PMF indeed presents lower coupling losses, and this makes it the most suitable solution for short-to-medium-distance links. Note that the constant coupling losses of the link have a greater impact than the group delay variation and attenuation.

To facilitate feasible communication connections, the PMF should possess the capability to create bends with a minimal curvature radius. The nonlinearity in how the propagation constant changes with the frequency leads to waveguide dispersion. Waves that propagate with a propagation constant similar to that of the cladding material have a field distribution mainly confined to the covering. Any disturbance in this field can cause the mode to transform locally into a radiating one, resulting in additional losses. An important scenario where these radiation losses occur is during bending, especially at lower frequencies (modes with lower propagation constants), as illustrated in Figure 6. Increasing the frequency enhances the guiding behavior of the PMF. In instances where small radii are involved in an application, the losses incurred during bending should be accounted for in the communication system's link budget.

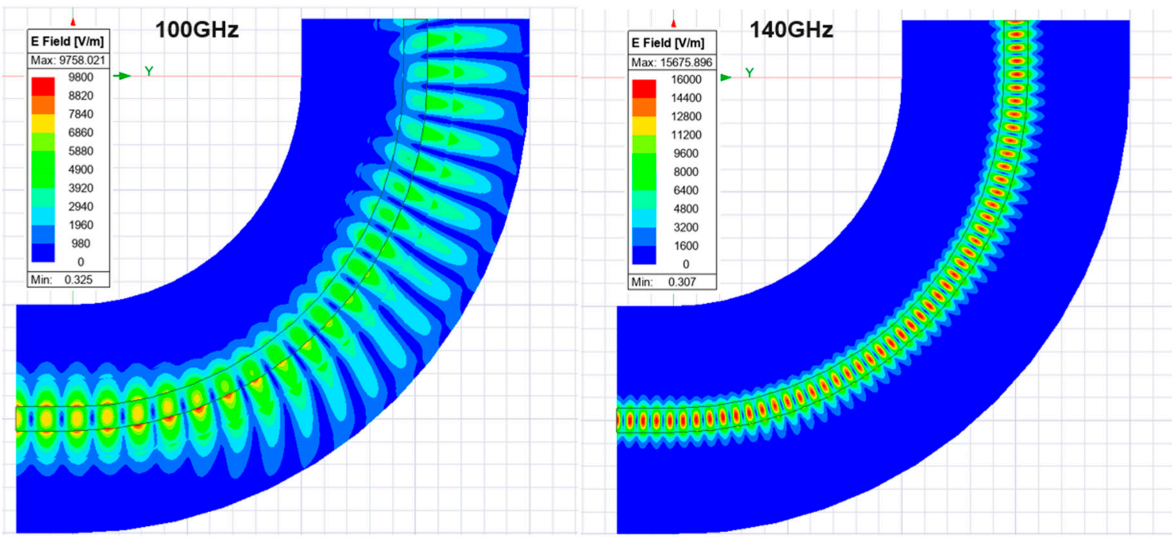

Figure 6. Simulation results in terms of the field distribution of a 90 deg bent PMF at 100 GHz and 140 GHz.

Following the investigation of the PMFs' propagation performance, we conducted additional simulations to investigate the effect of the metal coating or shielding of the PMF. In this context, the metal coating could be used to enable the electromagnetic isolation of the PMF from the surrounding environment, while keeping the propagating field confined to the PMF. However, a metal coating provides no benefit in a foam-cladded PMF since the cladding already shields the PMF core. On the other hand, if the foam cladding is bypassed and the PMF core is directly coated with metal, then the resulting waveguide is no longer a dielectric waveguide, as with the PMF, but a metallic waveguide with a polymer filling, which leads to much higher attenuation, as illustrated in Figure 7. Here, we simulated the hollow-core cylindrical PMF with a thin aluminum coating with a thickness of 700 nm, which is greater than the skin effect depth in the D-band (110–170 GHz).

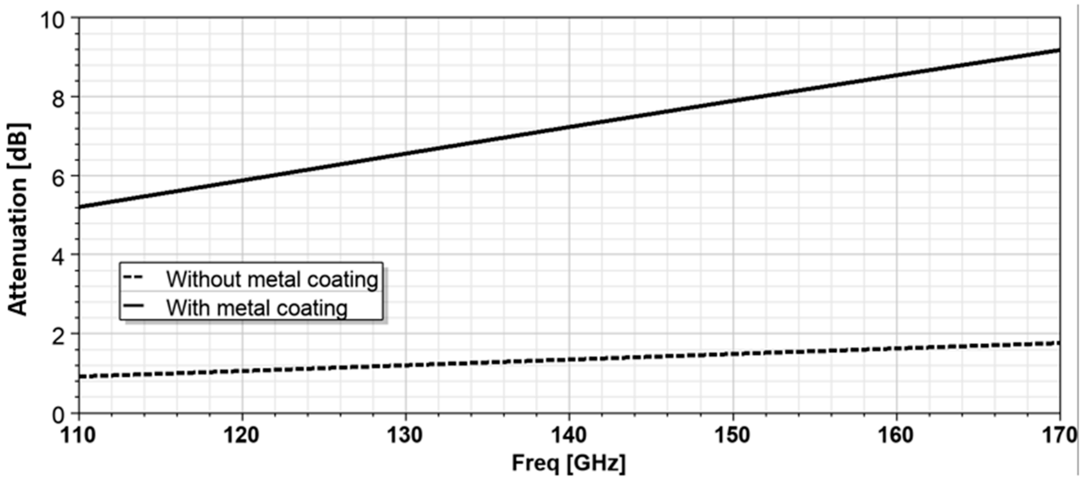

Figure 7. Simulation results in terms of the attenuation of the rectangular cross-section PMF with and without a metal coating.

3. PMF-AiP Coupling

RF-over polymer applications require coupling between the transceiver mm-wave IC (MMIC) and the PMF. Multiple solutions have been proposed in [6–10], such as MMIC couplers and on-chip antennas. A promising solution appears to be the antenna-in-package (AiP) [16], which is further investigated in this work.

Our proposed design provides an in-package solution for the IC-to-PMF coupling problem that does not suffer from electrical/mechanical performance issues, such as PMF displacement, while it is simple and cost-effective. For the implementation of this solution, the embedded wafer level ball grid array (eWLB) advanced packaging technology [28] is employed: a variation of a two-dimensional Vivaldi antenna is designed in the fan-out area of the eWLB, and the antenna is used to wirelessly couple the (packaged) IC to the PMF. The antenna was selected and designed to provide lateral radiation, so, instead of using a perpendicular configuration of the IC-PMF pair, a neat coplanar solution is provided. The solution is very simple and highly integrated: the IC readily connects to the antenna, taking advantage of the eWLB construction, so the coupling is merely achieved by the packaged IC, without the need for any extra interface. The implementation of the IC-to-PMF coupling is achieved without any extra cost and without compromising the performance.

The proposed structure implies the use of an antenna with high lateral directivity to ensure minimal coupling loss between the IC and the PMF. Although the term "antenna" implies a far-field analysis, it is important to mention that the proposed structure utilizes an antenna in near-field operation. As a result, optimization with the presence of the PMF is needed. The lateral antenna coupling offers low coupling losses and higher antenna–PMF alignment tolerance in comparison to perpendicular coupling. In addition, by utilizing a lateral coupling PMF, bending losses are fully avoided as no bending is required to turn the PMF to the correct direction for the application.

3.1. Packaging Technology Characterization

A key aspect of the coupling's performance is the electromagnetic behavior of the packaging technology. The packaging technology that was used for our design is the eWLB package [28–30]. In Figure 8, a cross-section of the packaging is shown. The coupling performance is mainly limited by the electromagnetic performance of the dielectric layers and the mold compound (dielectric characteristics), as well as the redistribution metals (conductivity and surface roughness).

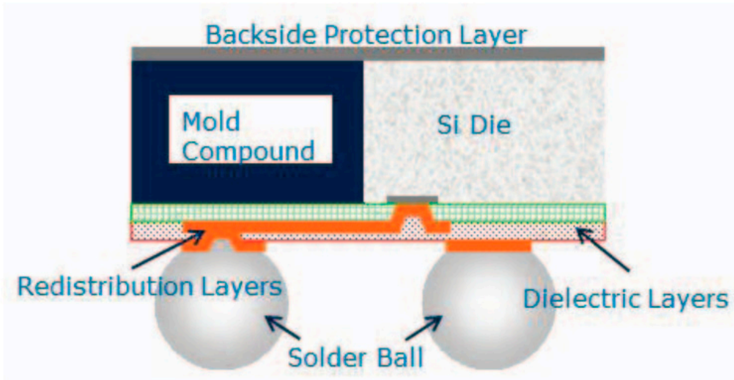

Figure 8. Cross-section of eWLB package [28].

Both the dielectric parameters of the mold compound and the dielectric layers and the surface roughness of the redistribution layer have a complex dependence on the frequency. As a result, the implementation of a simulation model for the complex dielectric constants and the surface roughness becomes a necessity.

The most suitable model to describe the performance of the eWLB's dielectrics is the Djordjevic–Sarkar model, which assumes frequency-dependent complex relative permittivity [28]:

$$\begin{aligned} \varepsilon(\omega) &= \varepsilon'(\omega) + \mathrm{j}\varepsilon''(\omega) \\ &= \varepsilon_\infty + \frac{\Delta\varepsilon}{\ln\left(\frac{\omega_B}{\omega_A}\right)} \ln\left(\frac{\omega_B + \mathrm{j}\omega}{\omega_A + \mathrm{j}\omega}\right) + \frac{\sigma}{\mathrm{j}\omega\varepsilon_0} \end{aligned} \quad (2)$$

where ε_∞ is the high-frequency relative permittivity, $\Delta\varepsilon = \varepsilon_{DC} - \varepsilon_\infty$ is the difference between the high-frequency and DC relative permittivity, ε_0 is the free-space permittivity, σ is the bulk conductivity, $\omega = 2\pi f$ is the angular frequency and ω_A and ω_B are the lower and higher transition frequencies, respectively. The loss tangent is calculated from complex $\varepsilon(\omega)$ as [28]

$$\tan\delta(\omega) = -\frac{\varepsilon''(\omega)}{\varepsilon'(\omega)} \quad (3)$$

After implementing this model in the EM simulator for the dielectric materials of the packaging technology, we simulated a frequency sweep to determine the performance of the packaging in the desired frequency band, i.e., 110 GHz to 170 GHz.

At high frequencies, the process imperfections of the redistribution layers (RDL) have an impact on the performance. More specifically, the surface roughness of the metal layers adds to the effective impedance of the passive components in the eWLB.

To illustrate the impact of the frequency dependence of the dielectric and metal layers, three cases of coplanar strip lines were simulated. The first case was simulated with constant dielectric parameters and no surface roughness; the second case used the Djordjevic–Sarkar model for the dielectric layers, but no surface roughness model; and the third case included both the Djordjevic–Sarkar model for the dielectric layers and the Grouse model for the surface roughness of the conductors. The |S21| for a 10-mm-long CPS line is shown in Figure 9. As illustrated, the surface roughness has a significant impact on the CPS insertion loss. Regarding the dielectric layers' modeling, the constant dielectric parameter layers exhibit poor performance with the CPS line, which illustrates the importance of a realistic model of the stackup's electrical parameters.

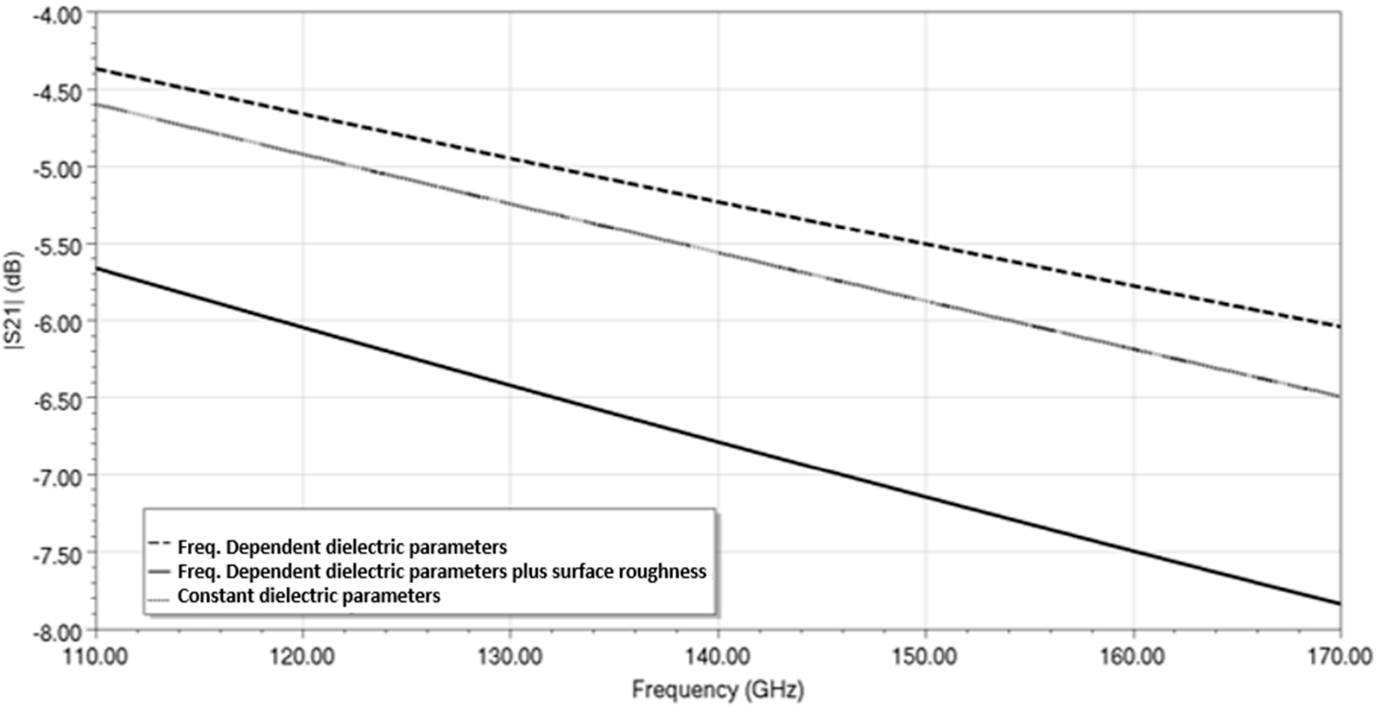

Figure 9. Simulation results in terms of the |S21| of a dual CPS for three eWLB modeling cases.

3.2. Coupler Design

The proposed solution for the coupling mechanism is based on the lateral coupling of the signal from the MMIC to the PMF. Multiple antenna structures are capable of lateral radiation, such as the bowtie antenna, the dipole antenna and more [4]. However, the application at hand requires high directivity in the lateral direction to minimize the coupling losses. The Vivaldi antenna is an ideal solution for this application. In principle, a Vivaldi antenna design requires multiple redistribution layers. However, in our work, a single-layer Vivaldi antenna is proposed, achieving lower manufacturing costs and complexity.

More specifically, the proposed antenna is a variation of the antipodal Vivaldi antenna [12,30], which utilizes three metal layers. However, the proposed design is implemented in the single redistribution layer of the eWLB stack-up. This implementation implies that the input of the antenna is differential (Figure 10), in contrast to a multiple-metal-layer process, where the input of the antenna can be single-ended.

Our antenna can be decomposed into three parts, namely the differential coplanar strip line (DCPS), the antenna body and the wave magnifier, which, in our proposed design, is an elliptic metal layer (Figure 10), although alternative shapes are also possible.

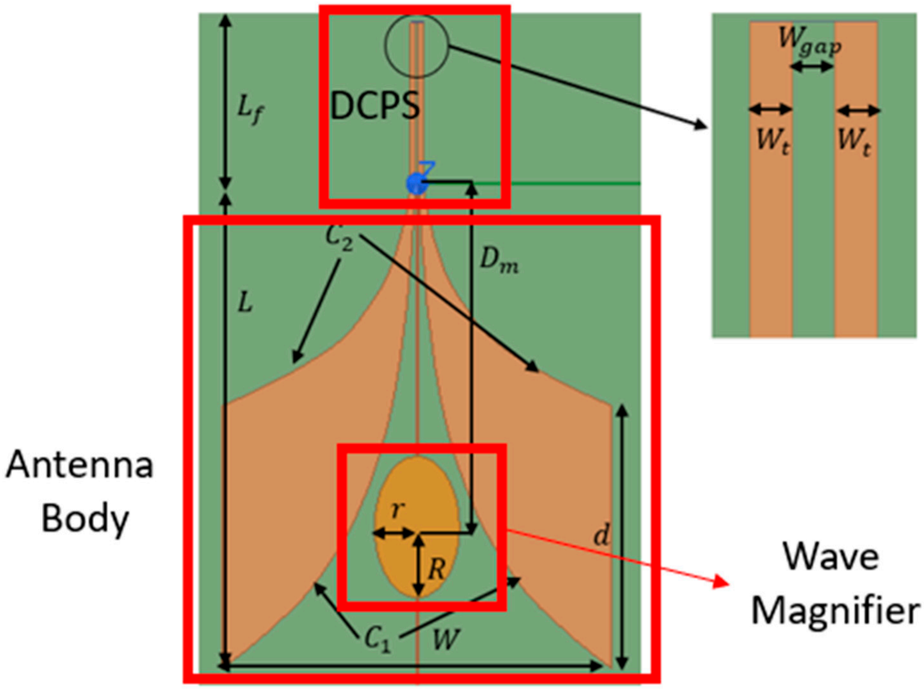

Figure 10. Single-layer antenna geometry.

The DCPS connects the Vivaldi slot to the IC and is matched at 100 Ohms differential impedance to ensure maximum power transfer. The thickness of each trace is standard and is predefined by the technology. The width of each trace, W_t, and the gap, W_{gap}, between the two traces affect the differential impedance of the strip line and its insertion losses.

The antenna body is composed of two RDL traces, as shown in Figure 10, with total length L. The total width of the Vivaldi slot is W and the length of the edge is d. By defining these three geometric parameters and taking into consideration that the gap between the two traces of the Vivaldi slot must be the same as the DCPS at the point where they are connected, we can define the curved edges of the two traces [4]:

$$\begin{gathered} C_1\ (t) = \pm 0.5 * W_{\mathrm{gap}} * exp(r_1\ t),\ \ 0 \le t \le L \\ C_2\ (t) = \pm\left(0.5 * W_{\mathrm{gap}} + W_{\mathrm{t}}\ \right) * \exp(r_2\ t) \\ 0 \le t \le L - d, \end{gathered} \tag{4}$$

where r_1 and r_2 are defined by the conditions $C_1(L) = W$ and $C_2(L-d) = W$. The role of the Vivaldi slot is to guide the incident wave from the DCPS to radiate laterally with the minimum possible scattering losses, which is not possible using a simple slot.

Finally, concerning the magnifier, its general shape is not important, although its dimensions and its position with respect to the antenna body are. By appropriately adjusting the geometric parameters of the magnifier, we can boost the radiating field in the desired direction. The magnetic field of the wave creates a secondary current source on the magnifier, which acts as a secondary radiator. The superposition of the primary and secondary waves increases the gain of the antenna. In Figure 11, the Poynting vector at the edge of the antenna with and without the magnifier is shown, illustrating the amplification of the electromagnetic field of the antenna with the magnifier. Figure 12 shows the 3D electric field distribution of the antenna with and without the magnifier, where we can clearly see the field intensity difference. The position and dimensions of the magnifier have an impact on the antenna's performance. We ran parametric simulations in HFSS to determine the optimal D_{m} and R parameters (Figure 10), while keeping the R/r ratio constant. The final decision for the magnifier was based on the result with the highest gain, without the presence of the PMF, since the results are transferable.

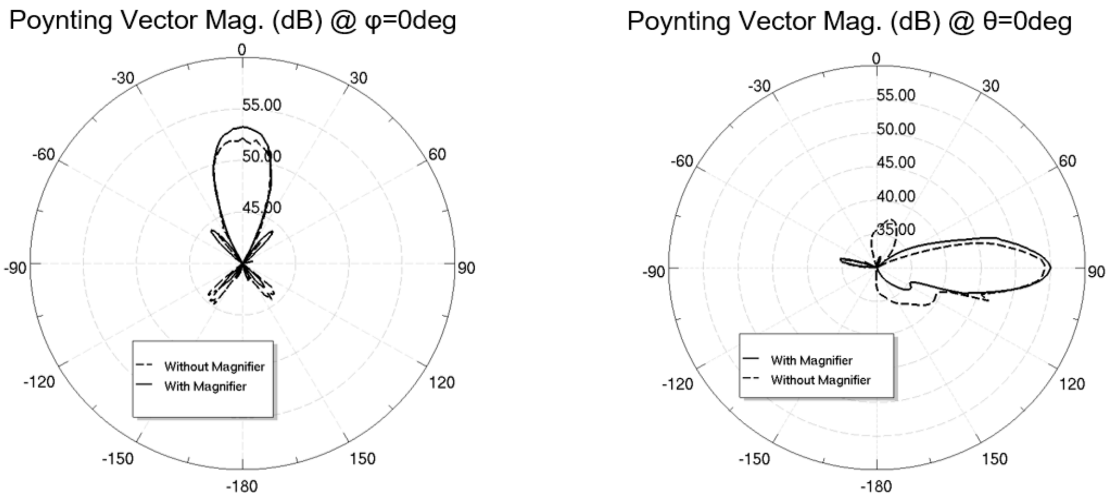

Figure 11. Simulation results for the Poynting vector magnitude pattern at 140 GHz.

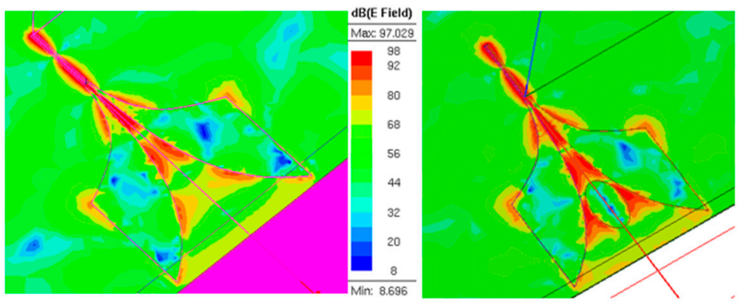

Figure 12. Simulation results in terms of the E-field 3D distribution without (**left**) and with (**right**) a magnifier at 140 GHz.

In Figure 13, the normalized E- and H-field patterns in dB are shown at 140 GHz. As illustrated, the antenna directs the electromagnetic field in the desired lateral direction.

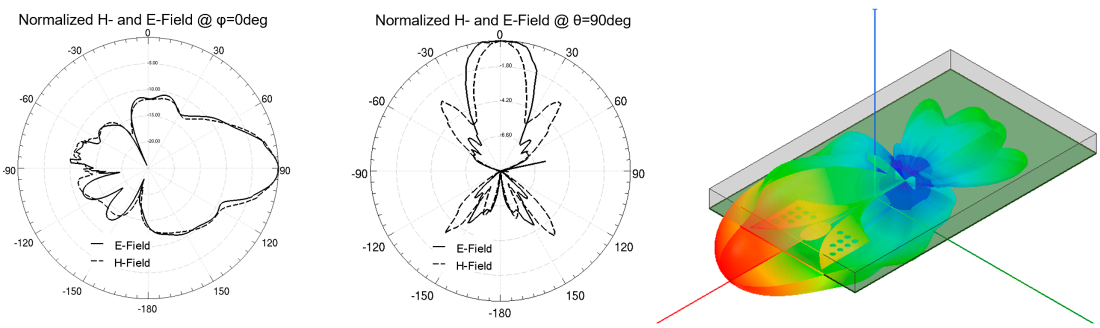

Figure 13. Simulation results in terms of the normalized H- and E-field patterns and the Poynting vector 3D graph without a PMF at 140 GHz (**left** to **right**).

Recall that the evaluation of the antenna's near-field characteristics without the presence of the PMF is not sufficient. The verification of the correct operation of the structure needs to be considered. For this purpose, the near-field characteristics in the presence of the PMF are re-evaluated, as well as the correct behavior of the electromagnetic wave, meaning that a propagating wave must be visible.

The PMF used for the evaluation of the antenna's near-field characteristics is the solid-core rectangular PMF that was discussed in the previous section. In Figure 14, the normalized E- and H-field patterns at 140 GHz are shown. It is clear that the PMF affects the antenna's performance.

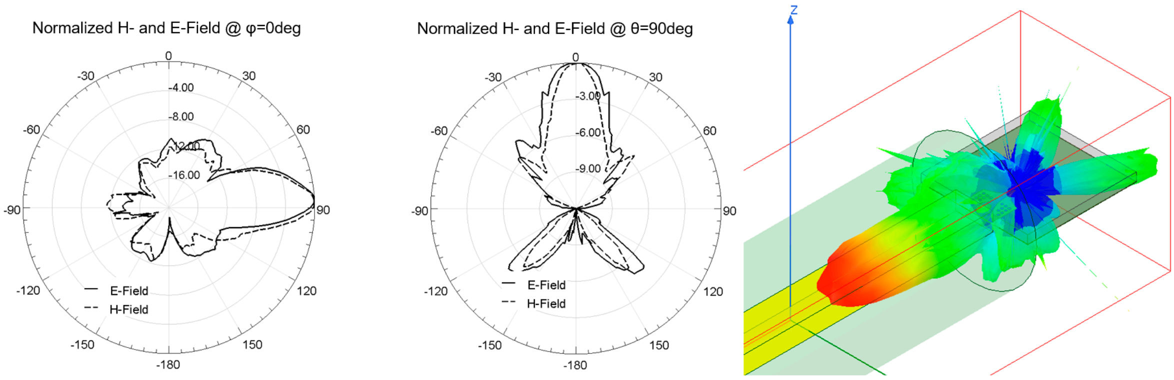

Figure 14. Simulation results in terms of the normalized H- and E-field patterns and the Poynting vector 3D graph with a PMF at 140 GHz (**left** to **right**).

Although the field patterns of the coupler structure are valuable, the most important performance metric of the coupler is the total coupling loss to the PMF. In Figure 15, the coupling losses for the four different PMF geometries are illustrated. As was expected from the analysis of the PMF characteristics, the solid-core rectangular PMF presents the lowest coupling loss. It is important to mention that the simulation results represent only the coupling losses of the structure. The antenna's input network insertion loss is not included and the PMF's propagation loss is de-embedded.

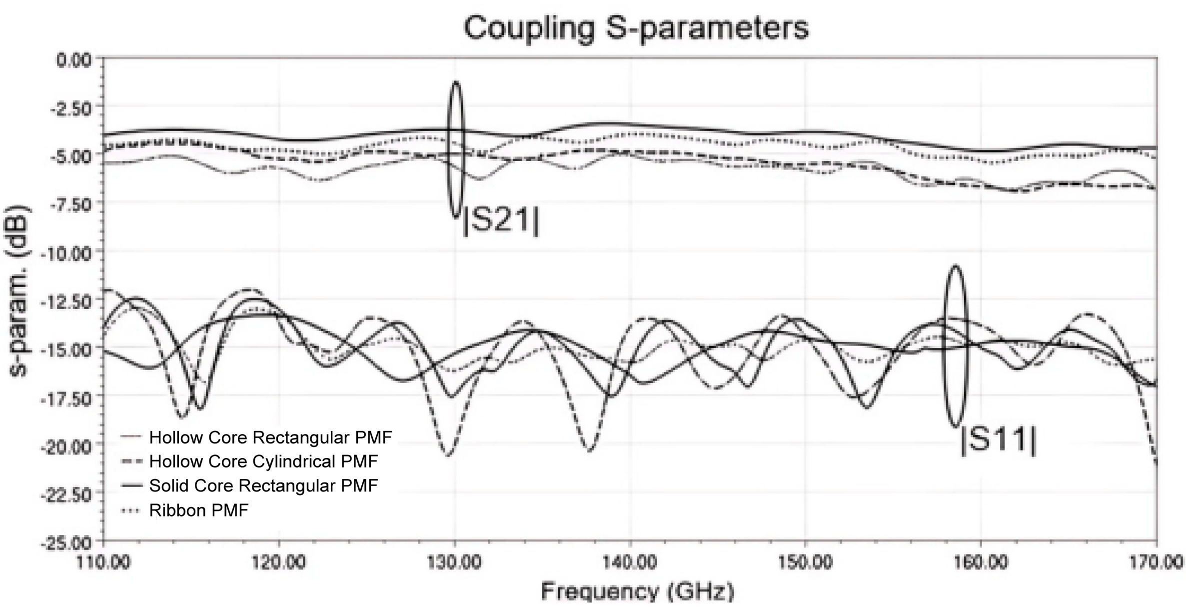

Figure 15. Coupling |S21| for the four PMF cases.

As mentioned earlier in this paper, an advantage of the Vivaldi antenna is that the input signal creates an electromagnetic field with a profile similar to the TE-like modes of the rectangular PMF. This effect is very beneficial for the overall performance, as it ensures single-mode operation. In other words, the Vivaldi antenna effectively suppresses the TM-like modes. This suppression is illustrated in Figure 16, where the TM-like modes are below −60 dB and the TE21 mode is approximately at −18 dB. To achieve this suppression, the proposed Vivaldi antenna requires only the differential mode of the dual coplanar strip line at the input network. The common mode not only does not suppress additional modes but also reduces the directivity of the antenna, as illustrated in Figure 17.

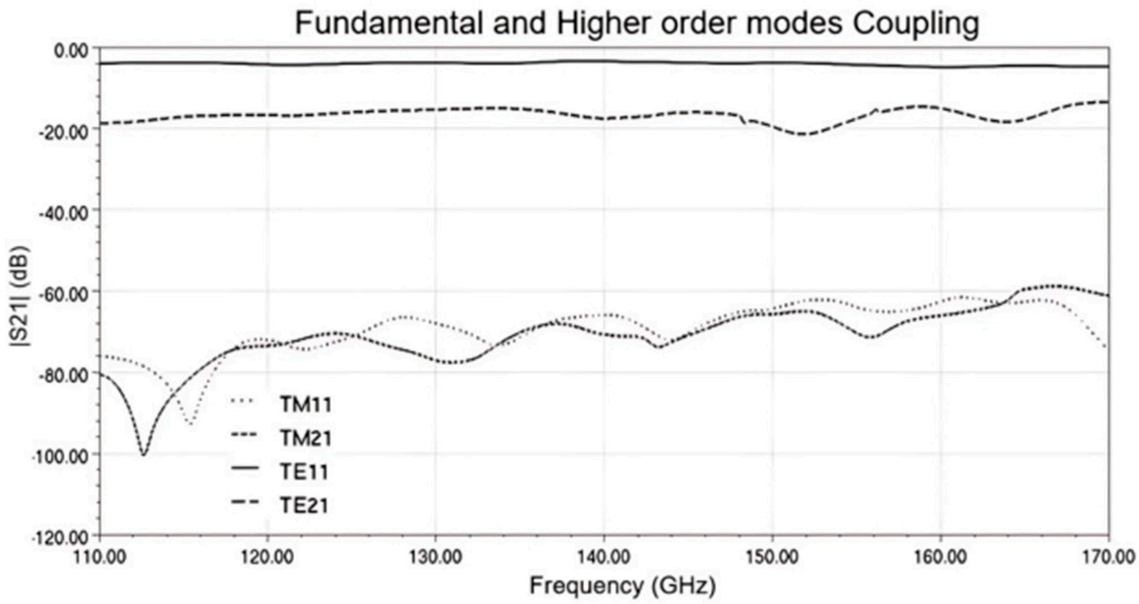

Figure 16. Coupling losses of the fundamental and higher-order modes of the solid rectangular PMF.

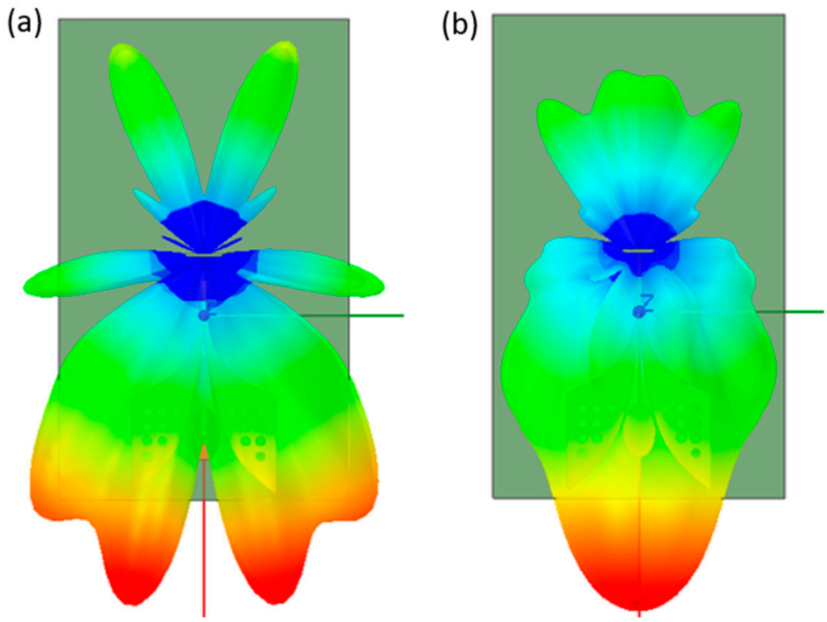

Figure 17. Poynting vector magnitude for (**a**) common mode and (**b**) differential mode of the differential coplanar strip line at 140 GHz.

A very important aspect of a wireless coupling structure for a PMF is the robustness of the coupling mechanism, i.e., the displacement tolerance of the PMF in front of the antenna. Due to the relatively small size of the package and the PMF, the precise placement of the PMF in front of the antenna is almost impossible. The proposed structure offers high tolerance regarding the PMF displacement of approximately 0.02 dB per 10 µm of displacement, as shown in Figure 18.

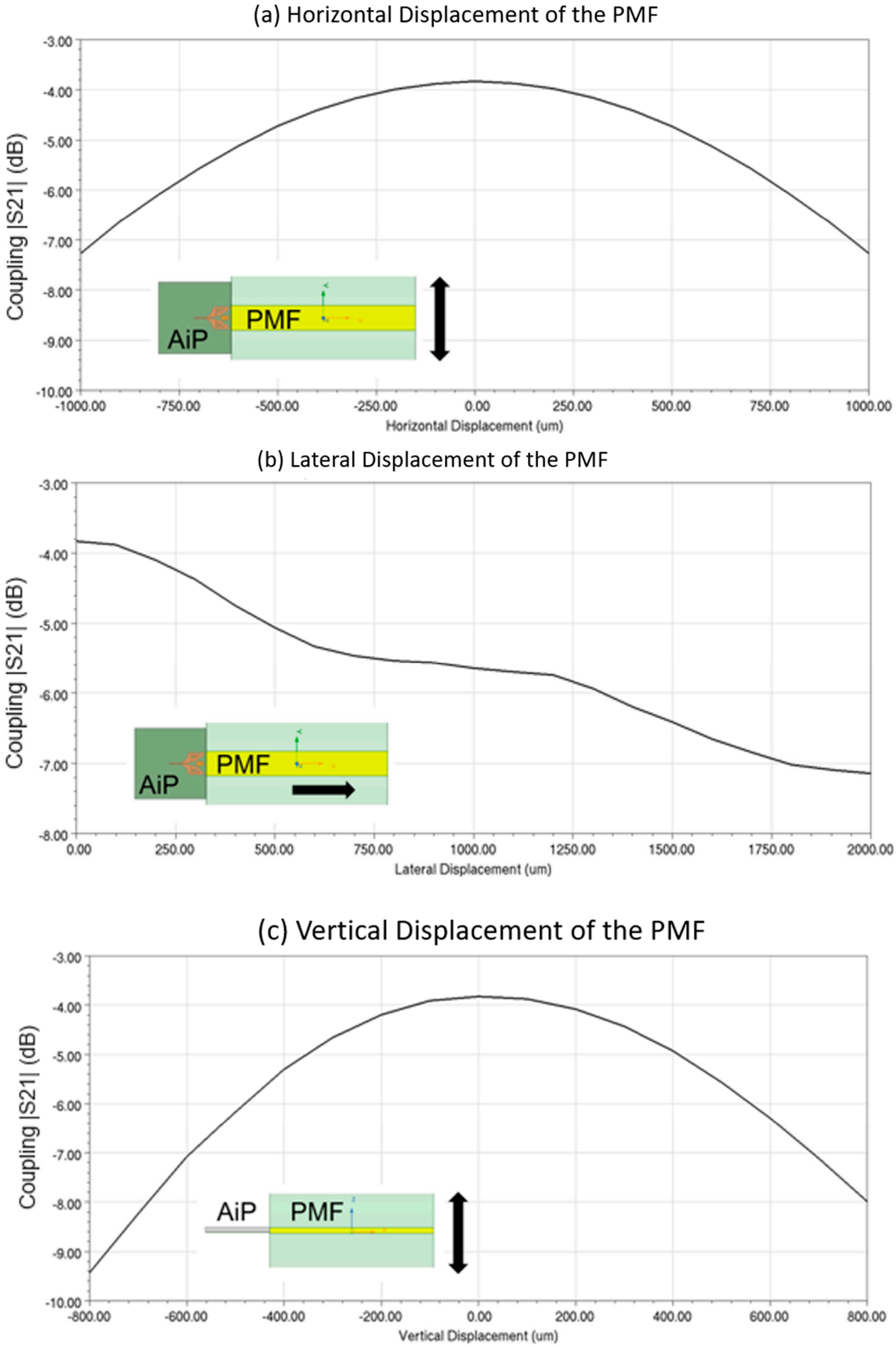

Figure 18. (**a**) Horizontal, (**b**) lateral and (**c**) vertical PMF displacement at 140 GHz.

4. AiP Implementation and Measurements

In this section, we present the measurement results for the proposed coupling structure, as well as the measurements of the sample PMF that was used.

For both measurements, a Keysight N5244B VNA with a WR8-based frequency extender up to 140 GHz was used (Keysight, Rosebery, NSW, Australia). Additionally, a WR8-to-WR6.5 interface was used to connect the WR8 waveguide port of the extender with the WR6.5-to-PMF adaptors, while the mismatch was calibrated with the corresponding TRL calibration kit provided by Keysight. In Figure 19, the full measurement setup is illustrated. Due to the setup with the WR6.5 and the WR8 waveguides, only the overlapping frequency region could be measured, i.e., 110 GHz to 140 GHz.

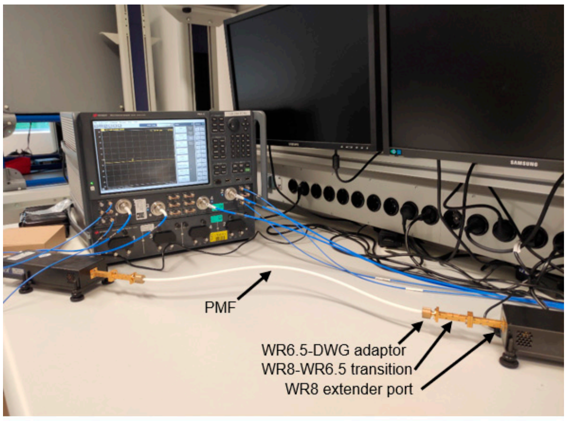

Figure 19. PMF measurement setup.

4.1. PMF Measurements

For measurement purposes, we used a solid-core cylindrical PMF with a 2.1-mm-diameter PE core and 6.4-mm-diameter PE foam cladding. In Figure 20, the insertion losses and group delays of three PMF samples are illustrated. The extrapolated insertion loss for the 1 m PMF is illustrated in Figure 21 with the adaptor losses de-embedded. The deviation between the measurements and simulation is due to additional factors that influence the measurement results, such as the excitation of the propagating modes. More specifically, in the measurement setup, the wave was excited directly in the core and the cladding of the PMF, due to the adaptors' shielding, thus neglecting the percentage of power propagating outside the PMF, which was considered in the simulations. In terms of the group delay, a GVD of approximately 2.1 ps per meter per GHz was calculated from all three measurements, which demonstrates the consistency of the measurements.

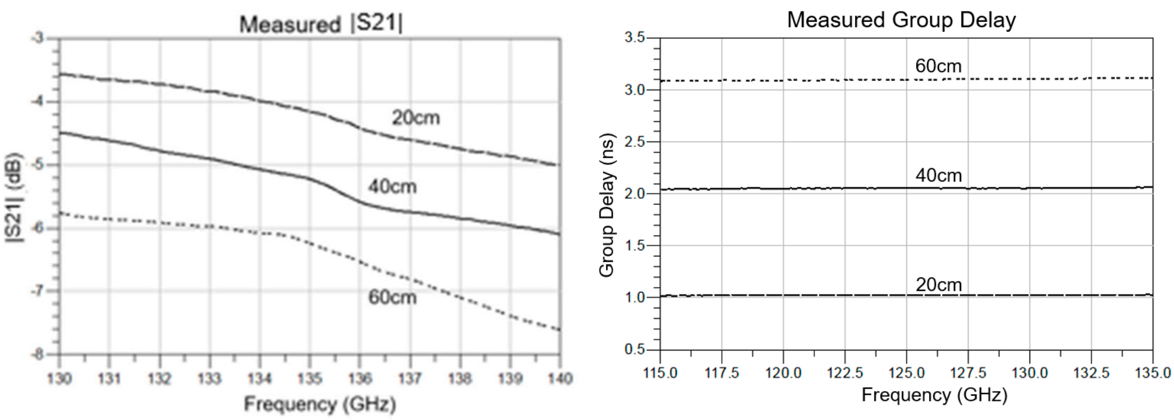

Figure 20. Measured |S21| and group delay of the PMF for different sample lengths.

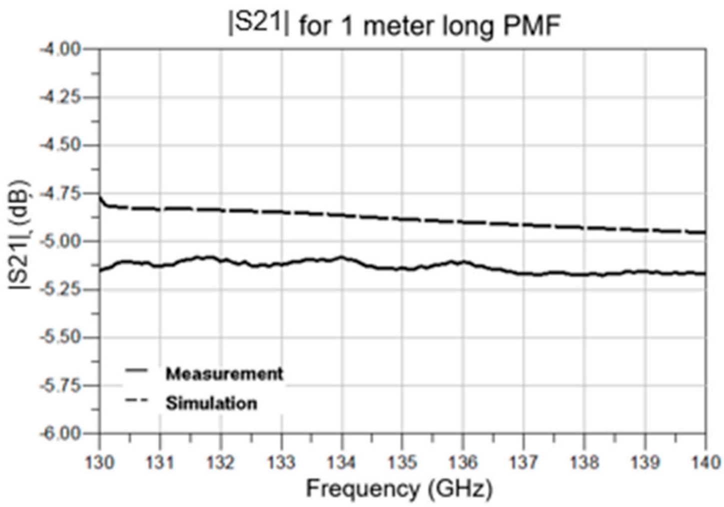

Figure 21. Simulated and measured |S21| at 1 m.

4.2. Coupler Measurement

To evaluate the antenna–coupler performance, a back-to-back antenna setup was designed and fabricated in order to simplify the hardware needed for the measurements. For the antenna's integration in the eWLB packaging technology, large metal areas were not allowed. For this reason, we introduced holes in the metal through cheesing. It is noteworthy that cheesing did not affect the antenna's performance. In Figure 22a, a photo of the back-to-back antennas is illustrated. The two antennas are connected through a 6 mm dual coplanar strip line. The concept of this design is to utilize two PMFs, which are connected to a VNA port each, and feed the antennas through their other side, as illustrated in Figure 22b.

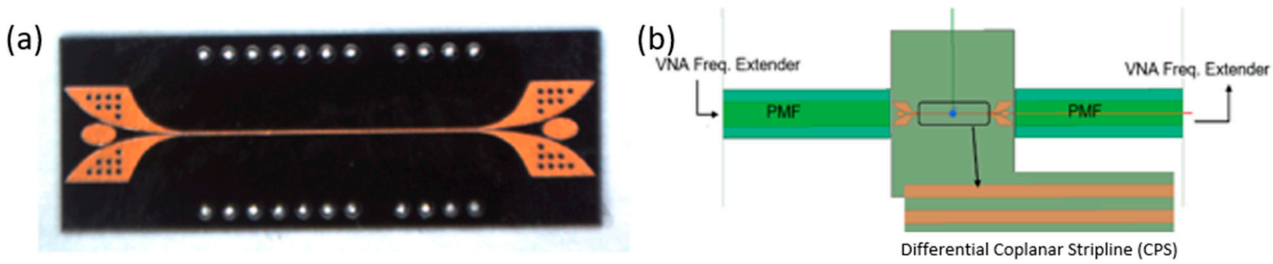

Figure 22. (**a**) Microscopic view of the back-to-back antennas and (**b**) measurement setup model in HFSS.

The coupling losses for a single antenna can then be easily calculated from the measured $|S_{21}|$ of the structure as follows:

$$\text{Cp.Loss} = [|S_{21}| - (\text{CPS Loss}) - 2 * (\text{PMF Loss})]/2 \quad (5)$$

At this point, it is important to mention again that the Vivaldi antenna suppresses the electromagnetic waves with electric fields perpendicular to its plane. However, such a field is produced by the extenders and is guided along the PMF, as shown in Figure 23. For this reason, the plane of the antenna needs to be parallel to the electric field of the extender and perpendicular to the plane of the working bench, as shown in Figure 24 on the right.

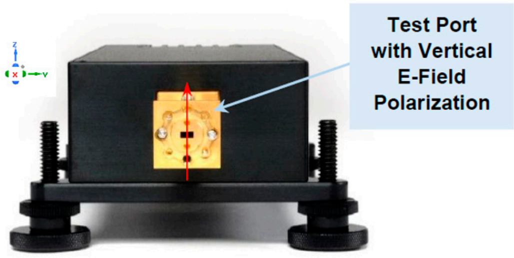

Figure 23. E-field of the extender module.

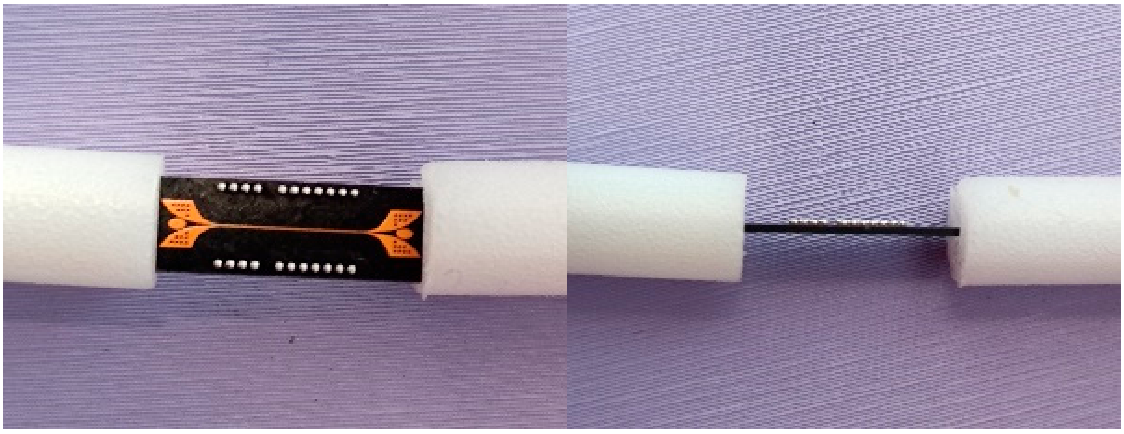

Figure 24. Antenna placement for measurement at 90 deg (**left**) and 0 deg (**right**).

For the antenna coupling measurements, 20-cm-long PMFs were used and carefully aligned with the antennas on the eWLB. As shown in Figure 25a, a good match between the measurements and simulations was obtained. Using Equation (5), the antenna coupling losses were calculated, as shown in Figure 25b.

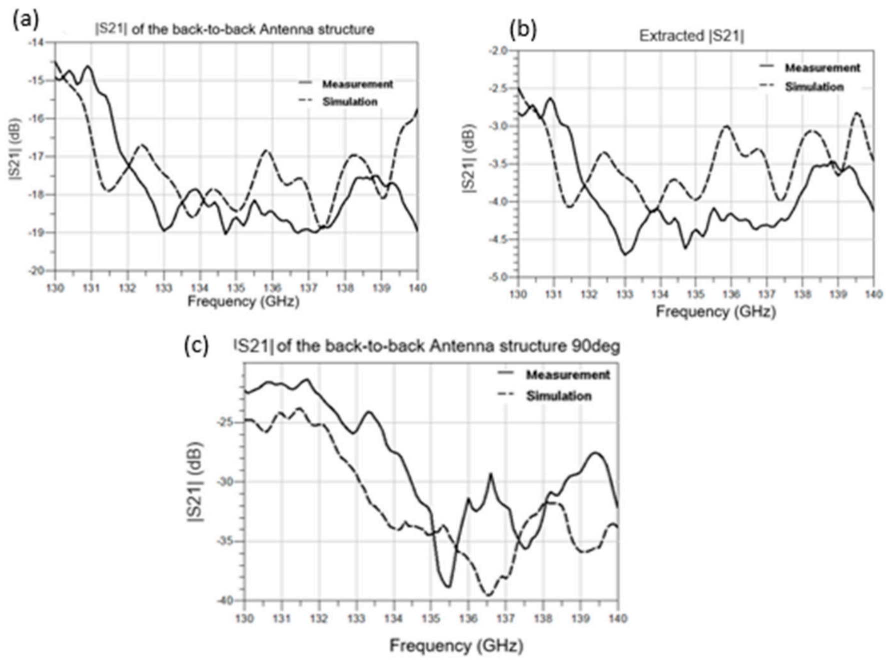

Figure 25. (**a**) |S21| of the back-to-back antenna structure, (**b**) antenna coupling losses and (**c**) |S21| of the back-to-back antenna structure rotated by 90 degrees.

At lower frequencies, low coupling loss is observed. This is a result of the weaker field confinement of the PMF, which leads to extra coupling between the two PMFs without the antenna. However, when rotating the antenna at 90 deg (Figure 24, left), the suppression of the electromagnetic field is observed through the much lower |S21| of the structure, as shown in Figure 25c. This proves that the coupling is mainly due to the antennas and not to power transfer over the air around the two PMF sections.

In conclusion, the proposed structure offers a very cost-efficient and robust solution with relatively low coupling loss (approximately 3.5 dB), while it presents high displacement tolerance. Its mechanical stability and high level of integration will be beneficial for many real-life applications.

A comparison between the state-of-the-art IC-PMF coupling solutions is shown in Table 2.

Table 2. Proposed coupler's performance against the literature.

Ref.	Coupling Type	Frequency (GHz)	Implementation	Coupling Loss (dB)
[8]	Wireless	60	On-Chip Antenna	6 (simulated)
[9]	Wireless	120	On-Chip Antenna	11 (measured)
[11]	Wireless	120	On-Chip Antenna	7.1 (simulated)
[10]	MMIC interface	120	PCB	3.4 (measured)
[12]	Wireless	140	PCB	3.5 (measured)
[16]	Wireless	130	Antenna-In-Package	3 (measured)
This work	Wireless	140	Antenna-In-Package	3.5 (measured)

5. Conclusions

PMF links offer a very good solution for medium-distance, high-data-rate links at sub-THz. By utilizing low-loss polymer materials, attenuation as low as 1 dB/m is possible. Additionally, the simulation results show that multimode operation not only does not worsen the overall group delay and thus the performance of the link, but it benefits the coupling, as a PMF with larger cross-section can be utilized, as long as the higher-order modes are suppressed, as illustrated in this paper. The modal and waveguide dispersion is optimized through the correct sizing of the PMF in the desired frequency of operation. However, dispersion compensation can be further implemented in the digital domain of the system [31] using our proposed design. In terms of the coupling mechanism, the link's flexibility offers a variety of coupling solutions that can be utilized. The less complex and cost-efficient antenna-in-package that we propose achieves an average coupling loss of 3.5 dB.

An important factor that is not covered in this paper is the temperature. Regarding eWLB structures, the temperature will not reduce the links' performance as presented in [29,30]. On the other hand, the PMF will be the bottleneck of the link in terms of the temperature impact. However, there are polymer materials available that can support high temperatures while presenting similar dielectric performance [24].

As a last remark, the eWLB technology enables the scalability of the proposed design to lower frequencies, making it a viable solution for a wide range of applications. A notable example is presented in [29], where the concept of an eWLB package-integrated circularly polarized antennas in the 57 GHz to 64 GHz ISM band is introduced. Additionally, in [30], various eWLB package-integrated antennas are introduced operating at 77 GHz, including a similar Vivaldi antenna to that presented in this paper. This scalability not only facilitates adaptation to different frequency bands but also enhances the potential for integration into future radar and communication systems, driving further advancements in the field.

Author Contributions: Conceptualization, V.L., M.W. and W.H.; Methodology, V.L. and Y.P.; Formal analysis, V.L.; Investigation, V.L.; Resources, Y.P.; Writing—original draft, V.L.; Writing—review & editing, Y.P.; Visualization, W.H.; Supervision, Y.P.; Project administration, Y.P., F.D. and M.W.; Funding acquisition, F.D. All authors have read and agreed to the published version of the manuscript.

Funding: This work was partially funded by the H2020-ICT-07-2018 Project No. 824962 "Car2TERA". Part of this work was funded by the European Union's Horizon Europe program under grant agreement No. 101096302 (6GTandem). The 6GTandem project has received funding from the European Union's Smart Networks and Services Joint Undertaking (SNS JU).

Institutional Review Board Statement: Not applicable.

Informed Consent Statement: Not applicable.

Data Availability Statement: The original contributions presented in this study are included in the article. Further inquiries can be directed to the corresponding author.

Conflicts of Interest: Franz Dielacher, Maciej Wojnowski and Walter Hartner were employed by the company Infineon Technologies AG. The remaining authors declare that the research was conducted in the absence of any commercial or financial relationships that could be construed as a potential conflict of interest.

References

1. Mattia, O.E.; Sawaby, M.; Zheng, K.; Arbabian, A.; Murmann, B. A 10-Gbps Continuous-Time Linear Equalizer for mm-Wave Dielectric Waveguide Communication. *IEEE Solid-State Circuit Lett.* **2020**, *3*, 266–269. [CrossRef]
2. Zhong, Q.; Chen, Z.; Sharma, N. 300-GHz CMOS QPSK Transmitter for 30-Gbps Dielectric Waveguide Communication. In Proceedings of the IEEE Custom Integrated Circuits Conference, San Diego, CA, USA, 8–11 April 2018.
3. Momson, I.; Dong, S.; Yelleswarapu, P. 315-GHz Self-Synchronizing Minimum Shift Keying Receiver in 65-nm CMOS. In Proceedings of the IEEE Symposium on VLSI Circuits, Honolulu, HI, USA, 16–19 June 2020.
4. Balanis, C.A. *Advanced Engineering Electromagnetics*; Wiley: Singapore, 2012.
5. Silicon Line GmbH. Available online: https://www.silicon-line.com/copper-cable-limitations/ (accessed on 1 February 2023).
6. De Vit, M.; Ooms, S.; Zhang, Y.; Reynaert, P. Polymer Microwave Fibers. *IEEE Microw. Mag.* **2020**, *21*, 51–66.
7. Dolatsha, N.; Chen, C.; Arbabian, A. Loss and Dispersion Limitations in mm-Wave Dielectric Waveguides for High-Speed Links. *IEEE Trans. Terahertz Sci. Technol.* **2016**, *6*, 637–640. [CrossRef]
8. Kim, Y.; Nan, L.; Cong, J.; Chang, M.-C. High-speed mm-wave datalink based on hollow plastic cable and cmos transceiver. *IEEE Microw. Wirel. Compon. Lett.* **2013**, *23*, 674–676. [CrossRef]
9. Reynaert, P.; Tytgat, M.; Volkaerts, W.; Standaert, A.; Zhang, Y.; Wit, M.D. Polymer Microwave Fibers: A blend of RF copper and optical communication. In Proceedings of the European Solid-State Circuits Conference, Lausanne, Switzerland, 12–15 September 2016.
10. Van Thienen, N.; Reynaert, P.; Zhang, Y.; De Wit, M. An 18 Gbps polymer microwave fiber (PMF) communication link in 40nm CMOS. In Proceedings of the European Solid-State Circuit Conference, Lausanne, Switzerland, 12–15 September 2016.
11. Thienen, N.; Reynaert, P. A 120GHz In-Band Full-Duplex PMF Transceiver with Tunable Electrical-Balance Duplexer in 40nm CMOS. In Proceedings of the IEEE European Solid State Circuits Conference, Leuven, Belgium, 11–14 September 2017.
12. Dens, K.; Vaes, J.; Ooms, S.; Wagner, M.; Reynaert, P. A PAM4 Dielectric Waveguide Link in 28 nm CMOS. In Proceedings of the IEEE European Conference on Solid-State Circuits, Grenoble, France, 13–22 September 2021.
13. Standaert, A.; Reynaert, P. Analysis of Hollow Circular Polymer Waveguides at Millimeter Wavelengths. *IEEE Trans. Microw. Theory Tech.* **2016**, *64*, 3068–3077. [CrossRef]
14. De Wit, M.; Zhang, Y.; Reynaert, P. Analysis and Design of a Foam-Cladded PMF Link With Phase Tuning in 28-nm CMOS. *IEEE J. Solid-State Circuits* **2019**, *54*, 1960–1969. [CrossRef]
15. Dolatsha, N.; Arbabian, A. Dielectric Waveguide with Planar Multi-Mode Excitation for High Data-Rate Chip-to-Chip Interconnects. In Proceedings of the IEEE International Conference on Ultra-Wideband, Sydney, Australia, 15–18 September 2013.
16. Sawaby, M.; Dolatsha, N.; Grave, B.; Chen, C.; Arbabian, A. A Fully Packaged 130-GHz QPSK Transmitter With an Integrated PRBS Generator. *IEEE Solid-State Circuit Lett.* **2018**, *1*, 166–169. [CrossRef]
17. Meyer, A.; Schneider, M. Signal distortions in circular dielectric waveguides at mm-wave frequencies. *Int. J. Microw. Wirel. Technol.* **2021**, *14*, 8–18. [CrossRef]

18. Holloway, J.W.; Boglione, L.; Hancock, T.M.; Han, R. A Fully Integrated Broadband Sub-mmWave Chip-to-Chip Interconnect. *IEEE Trans. Microw. Theory Tech.* **2017**, *65*, 2373–2386. [CrossRef]
19. Volkaerts, W.; Thienen, N.V.; Reynaert, P. 10.2 An FSK plastic waveguide communication link in 40nm CMOS. In Proceedings of the IEEE International Solid-State Circuits Conference, San Francisco, CA, USA, 22–26 February 2015.
20. Rougier, B.; Aubert, H.; Lefrançois, A. Measurement of Shock Wave and Particle Velocities in Shocked Dielectric Material from Millimeter-Wave Remote Sensing. In Proceedings of the 2018 48th European Microwave Conference (EuMC), Madrid, Spain, 23–27 September 2018; pp. 855–858. [CrossRef]
21. Lou, Z.; Jian-Ming, J. Modeling and Simulation of Broad-Band Antennas Using the Time-Domain Finite Element Method. *IEEE Trans. Antennas Propag.* **2005**, *53*, 4099–4110.
22. Bao, H.; Nielsen, K.; Bang, O.; Jepsen, P.U. Dielectric tube waveguides with absorptive cladding for broadband, low-dispersion and low loss THz guiding. *Sci. Rep.* **2015**, *5*, 7620. [CrossRef]
23. Krishnamoorthy, A.V.; Goossen, K.W.; Jan, W.; Zheng, X.; Ho, R.; Li, G.; Rozier, R.; Liu, F.; Patil, D.; Lexau, J.; et al. Progress in Low-Power Switched Optical Interconnects. *IEEE J. Sel. Top. Quantum Electron.* **2011**, *17*, 357–376. [CrossRef]
24. Oliver, G. *Low-Loss Materials in High Frequency Electronics and the Challenges of Measurement*; DuPont: Wilmington, DE, USA, 2015.
25. Yeh, C.; Shimabukuro, F.I. *The Essence of Dielectric Waveguides*; Springer: Berlin/Heidelberg, Germany, 2008.
26. Stratton, J.A. *Electromagnetic Theory*; McGraw-Hill Book Company: New York, NY, USA, 1941.
27. Marcatili, E.A.J. Dielectric Rectangular Waveguide and Directional Coupler for Integrated Optics. *Bell Syst. Tech. J.* **1969**, *48*, 2071–2102. [CrossRef]
28. Huynh, N.H.; Saverio, T.; Wojnowski, M.; Haubner, G.; Pahlke, S.; Schmitt, J.; Mayr, H.; Würtele, J.; Rueddenklau, U.; Nasr, I.; et al. eWLB package for millimeter wave application. In Proceedings of the 2015 European Microelectronics Packaging Conference (EMPC), Friedrichshafen, Germany, 14–16 September 2015; pp. 1–5.
29. Schmidbauer, P.; Wojnowski, M.; Weigel, R.; Hagelauer, A. Wafer Level Package Integrated Antenna Concepts for Circular Polarization. In Proceedings of the 2018 IEEE 27th Conference on Electrical Performance of Electronic Packaging and Systems (EPEPS), San Jose, CA, USA, 14–17 October 2018.
30. Wojnowski, M.; Lachner, R.; Bock, J.; Wagner, C.; Starzer, F.; Sommer, G.; Pressel, K.; Weigel, R. Embedded wafer level ball grid array (eWLB) technology for millimeter-wave applications. In Proceedings of the 2011 IEEE 13th Electronics Packaging Technology Conference, Singapore, 7–9 December 2011; pp. 423–429. [CrossRef]
31. Hassona, A.; Vassilev, V.; He, Z.S.; Mariotti, C.; Dielacher, F.; Zirath, H. Silicon taper-based D-band chip to waveguide interconnect for millimeter-wave systems. *IEEE Microw. Compon. Lett.* **2017**, *27*, 1092–1094. [CrossRef]